Full Length Article

Removal of secondary phases and its effect on the transport behavior of $Cu_2ZnSn_{1-x}Ge_xS_4$ kesterite nanoparticles

Francisco Enrique Cancino-Gordillo, José-Luis Ortiz-Quiñonez, Mou Pal, Rutilo Silva González, Umapada Pal [*]

Instituto de Física, Benemérita Universidad Autónoma de Puebla, Apdo. Postal J-48, Puebla, Pue. 72570, Mexico

A B S T R A C T

Hole-transporting materials are very important for achieving high efficiency in perovskite solar cells. Thin films made of $Cu_2ZnSn_{1-x}Ge_xS_4$ have attracted the attention of researchers due to their potential as hole-transporting layers. However, defects and impurities define their effectiveness in solar cells. In this work, we present a facile wet chemical approach to remove the ZnS and Cu_8GeS_6 impurities from small (~11 nm) $Cu_2ZnSn_{1-x}Ge_xS_4$ (x = 0.0 to 0.7) nanoparticles synthesized by a hydrothermal process. The wet chemical process converted the nanostructures Cu-rich Zn-poor from their initial Zn-rich Cu-poor stoichiometry. Moreover, the bandgap energies of the nanostructures were reduced by about 0.1 eV after chemical treatment due to change the oxidation state of Cu from Cu^{1+} to Cu^{2+}. The kesterite films prepared by spin coating of chemically treated nanoparticle inks revealed enhanced electrical conductivity and hole concentration in comparison to the films prepared using untreated nanoparticle inks. While the highest hole concentration of about 6.52×10^{18} cm^{-3} was obtained for the films made of $Cu_2ZnSn_{1-x}Ge_xS_4$ nanoparticles with the highest x value (x = 0.7), the highest hole mobility (18.9 cm^{2}V^{-1}s^{-1}) was achieved for x = 0.3. The effects of secondary phase elimination on carrier concentration and mobility variation have been discussed.

1. Introduction

Quaternary chalcogenide Cu_2ZnSnS_4 (CZTS) is one of the most attractive materials for absorber layers of thin-film-based photovoltaic devices, with the potential of replacing conventional absorber materials such as CdTe and $CuIn_xGa_{1-x}S_2$ (CIGS), which contain toxic, scarce or costly elements like Cd and In. Apart from its non-toxic constituents, CZTS exhibits a high optical absorption coefficient (~10^4 cm^{-1}) in the visible spectra range, intrinsic p-type conductivity, and direct bandgap energy close to 1.5 eV [1,2], which are some essential features of a material to be used in the absorber layers of photovoltaic devices. In fact, by utilizing kesterite absorber layers containing sulfur (CZTS) and selenium (CZTSe), the power conversion efficiency of solar cells could be achieved up to 11.8% [3] and 12.6 % [4], respectively. However, those values are considerably lower in comparison to the power conversion efficiency (>20%) of the solar cells fabricated using CIGS [2,5]. One of the principal reasons for lower conversion efficiency or large open-circuit voltage (V_{oc}) deficit of CZTS-based solar cells is the presence of electronic defects in off-stoichiometric (i.e., Cu/(Zn + Sn) < 1 and Zn/

Sn > 1) CZTS, affecting its electrical and optical properties [6].

On the other hand, due to p-type conduction and moderate resistivity, recently CZTS thin films have been utilized as hole-transporting layers (HTLs) in perovskite solar cells (PSC), replacing conventional hole transporting layers such as PEDOT:PSS and spiro-OMETAD, which suffer from high cost, poor environmental and current-voltage (I-V) stabilities [7,8]. For utilization as absorber layer, the CZTS films should have a high absorption coefficient, high environmental stability, low cost, low defect content, and a direct bandgap in the range of 1.4–1.5 eV, which overlaps with the bandgap value (~1.35 eV) of the ideal semiconductor for single-junction solar cells [9,10]. Meanwhile, for utilization as HTL, apart from p-type conductivity, the CZTS films should have low resistivity, high hole mobility, and low electronic defect contents [11]. Wu et al. utilized CZTS film made of corresponding nanoparticle ink, as HTL in an n-i-p configured perovskite ($CH_3NH_3PbI_3$) solar cell and compared the performance of the device with the performance of a PSC fabricated with spiro-OMeTAD-based HTL [12], demonstrating the HTL made of CZTS nanoparticles can transport holes as effectively as commonly used HTLs such as spiro-OMeTAD. They observed a decrease in fill factor (*FF*)

from 65% using spiro-OMeTAD to 58.7% using CZTS for the PSC fabricated with CZTS nanoparticle-based HTL and associated to an increase in series resistance (R_s) of the device. On the other hand, a higher J_{sc} in the cell fabricated with CZTS nanoparticle ink was associated to the improved light absorption of the perovskite solar cell in the 400–850 nm spectral range and improved interfacial contact between the perovskite layer and Au electrode, which reduces the charge carrier (electron-hole) recombination. On the other hand, Yuan et al. utilized CZTS quantum dots for HTL in n-i-p configured perovskite (CH$_3$NH$_3$PbI$_3$) solar cells [13]. The CZTS quantum dots were synthesized using a hot injection method, and their bandgap was tuned by replacing sulfur with selenium. Substitution of S with Se reduced the resistivity of the kesterite HTL substantially (112.3 Ω•cm to 4.56 Ω•cm). The PSC fabricated with CZTSe as HTL exhibited a lower V_{oc} (0.808 V) than the PSC fabricated with CZTS (0.945 V), which was attributed to the reduction of bandgap energy from 1.64 eV (for CZTS) to 1.14 eV (for CZTSe). The reduction of bandgap energy in CZTSe is associated with an up-shift of its valence band edge, which induces higher recombination of charge carrier at the perovskite/HTL interface [13]. Therefore, for applying CZTS in PSCs, it must be grown under such conditions that reduce its resistivity, conserve the high light absorption capacity, and increase the bandgap to get a favorable alignment with the valence band of the perovskite layer.

As has been mentioned earlier, the compositional stoichiometry of CZTS affects its electrical and optical properties due to the formation of point defects such as Cu$_{Zn}$, Sn$_{Zn}$, V$_{Cu}$, and defect complexes [1,2,14]. One of the principal defects present in CZTS kesterite is the Sn$_{Zn}$ antisite. Due to low formation energy, the Sn$_{Zn}$ antisites produce (2Cu$_{Zn}$ + Sn$_{Zn}$) defect complex, which acts as a deep-level recombination center for electron-hole pairs or causes strong electron trapping [15–17]. Moreover, as Sn is a multivalent element, its oxidation state can interchange between Sn^{4+} and Sn^{2+} spontaneously due to the perturbation of charge balance in crystal lattice during the generation of photoinduced charge carriers. The reduction of Sn (Sn^{4+} to Sn^{2+}) can occur either in its native crystallographic position (Sn$_{Sn}$) or when Sn^{4+} is in an antisite defect. In both the cases, it can generate defect states in the bandgap which act as traps for electrons and holes [18]. Therefore, for applying CZTS in solar cells, it must be grown under specific conditions that reduce the concentration of Sn$_{Zn}$ antisite defects and inhibits Sn^{4+} ↔ Sn^{2+} transition.

The Cu$_{Sn}$, Cu$_{Zn}$ and Sn$_{Zn}$ antisite defects are easily formed in stoichiometric composition due to their low formation energies. One of the convenient ways to reduce the concentration of antisite defects in CZTS is by performing its synthesis under Cu-poor and Zn-rich condition (i.e., Cu/(Zn + Sn) ≈ 0.8 and Zn/Sn ≈ 1.2). This condition reduces the concentration of the antisite defects, enhancing the PCE of the fabricated solar cells [15–17]. However, according to the phase diagram of CZTS, the single kesterite phase is difficult to achieve due to the narrow composition region where the pure CZTS kesterite phase can be formed [19,20]. Consequently, several secondary phases (e.g., ZnS, Cu$_{2-x}$S and Cu$_2$SnS$_3$) are formed during the growth of CZTS and its post-growth processing [14,20–23]. One of the principal secondary phases formed during CZTS growth is ZnS [20,23], which is a high-resistive semiconductor with wide bandgap energy (3.84 eV). Presence of the ZnS phase reduces the active area for generating electron-hole pairs and current collection, along with an increase in series resistance of the device [14,20]. Thus, it is necessary to search for the ways to reduce the antisite defects, especially the defects associated with the unusual occupation of Sn atoms in the kesterite lattice and get rid of the secondary phases. In this regard, a partial substitution of Cu, Zn and Sn cations in kesterite lattice with other cations such as Ag$^+$ [24–26], Cd^{2+} [27,28] and Ge^{4+} [29–33], respectively, has been explored. For example, the partial substitution of Cu$^+$ by Ag$^+$ in the kesterite lattice was seen to diminish the concentration of antisite defects such as Cu$_{Zn}$ and Zn$_{Cu}$ and related defect complexes (i.e., V$_{Cu}$ + Zn$_{Cu}$, Cu$_{Zn}$ + Sn$_{Zn}$, and 2Cu$_{Zn}$ + Sn$_{Zn}$). In addition, formation of Ag$_{Zn}$, (Ag$_{Zn}$ + Zn$_{Ag}$) and (2Ag$_{Sn}$ + Sn$_{Zn}$) antisite defects in the Ag-substituted kesterite is not

expected because the Ag ions have unique + 1 valence state and their ionic radius (1.14 Å) is substantially larger than the ionic radii of Cu$^+$ (0.74 Å) and Zn^{2+} (0.74 Å) ions [34]. On the other hand, when the Cd^{2+} (0.92 Å) substitutes the Zn^{2+} cation to form the Cu$_2$Cd$_x$Zn$_{1-x}$SnS$_4$, the formation energy of Cu$_{Cd}$ and Cd$_{Cu}$ antisite defects in the kesterite is expected to be high due to the significant difference in the ionic radii and valance state of the two atoms [34].

A partial substitution of Sn by Ge has been seen to improve the V_{oc} of solar cells fabricated using CZTS as an absorber material [29–33]. Incorporation of Ge atoms substituting Sn in CZTS causes the formation of Cu$_2$ZnSn$_{1-x}$Ge$_x$S$_4$ (CZTGS) and reduces the possibility of formation of undesired defects such as Sn$_{Zn}$. The concentration of Sn$_{Zn}$ antisite defects decreases in CZTGS, as the energy of formation of such defects increases due to the tetravalent Ge^{4+} ion, which cannot exchange crystallographic sites with the cations such as Zn^{2+} and Cu$^+$, as occurs in the Sn case [35,36]. However, obtaining CZTGS with single kesterite phase is difficult as a high concentration of Ge (x ≥ 0.25) in CZTGS can generate tetragonal (kesterite) and orthorhombic mixed phase [37], segregation of secondary phases such as ZnS and Cu$_x$S (x ≥ 0.8) [38], or generate deep-level defects due to the formation of Sn vacancies (V$_{Sn}$) [36,39]. Moreover, the power conversion efficiency of the solar cells fabricated using CZTGS absorber layers containing larger Ge mol fractions of Ge (x > 0.25) is seen to reduce from 11 % (for × ≈ 0.25) to 1 % (for × ≈ 0.75) [40]. Therefore, while eliminating secondary phases in CZTGS is an essential task for applying it in solar cell, a systematic study of the impact of defects and secondary phases on the transport behaviors of CZTGS is very important for utilizing CZTGS nanostructures in the hole transporting layers of PSCs. Some specific chemical treatment processes have been applied by the researchers for the selective removal of secondary phases from CZTS and CZTSe films. For example, Buffière et al. utilized KCN treatment (carried out for 120 s at 20 °C using 5 wt% KCN aqueous solution in 0.5 wt% KOH) for removing Cu$_{2-x}$Se, Se^0, Cu$_x$SnSe$_y$, SnSe$_2$ and SnO$_2$ secondary phases from the surface of CZTSe thin films [41]. On the other hand, Fairbrother et al. utilized dilute HCl solution (10 % v/v at 75 °C for 300 s) for etching out ZnS phase from CZTS thin films [42]. Mousel et al. used HCl and Br$_2$-MeOH solutions to remove ZnSe and Cu$_2$SnSe$_3$, respectively, from CZTSe film surface [43]. Nevertheless, while the formation of secondary phases in CZTGS nanostructures and thin films has been reported by several research groups [29,32,33,37,38], utilization of chemical treatment for etching out secondary phases from CZTGS films or nanostructures has not been explored so far.

In this article, we present a chemical treatment process for eliminating secondary phases from the CZTGS (from x = 0.0 to 0.7) nanoparticles synthesized by hydrothermal process. The effect of the wet-chemical treatment on the elimination of secondary phases and its impact on the structural and optical properties of the nanostructures have been studied. Electrical properties of the films fabricated using those secondary phase-eliminated nanoparticles were evaluated by measuring their resistivity and Hall coefficient. We demonstrate that removal of secondary phases such as Cu$_8$GeS$_6$ and ZnS improves the electrical transport behaviors of CZTGS films, without affecting their microstructural and optical behaviors significantly.

2. Experimental

2.1. Reactive & solvents

Copper acetate hydrate (Cu(CH$_3$COO)$_2$·H$_2$O, ≥98%), tin chloride pentahydrate (SnCl$_4$·5H$_2$O, 98%), germanium tetrachloride (GeCl$_4$, 99.9999%), ethylenediamine (C$_2$H$_8$N$_2$, ≥98%), hexanethiol (C$_6$H$_{14}$S, 95%), and acetone (C$_3$H$_6$O, ≥99.5%) were purchased from Sigma-Aldrich, Mexico. Zinc acetate dihydrate (Zn(CH$_3$COO)$_2$·2H$_2$O, 99%), potassium hydroxide pellets (KOH), and sublimed sulfur powder (S, 99.95%) were acquired from J.T. Baker and Fermont, respectively. Hydrochloric acid (HCl) was purchased from CTR scientific, Mexico. All

the reagents were utilized as received, without further purification. Deionized (DI) water from a Millipore system ($\rho > 10^{18}$ Ω-cm) was used for the synthesis of the nanostructures.

2.2. Fabrication of $Cu_2ZnSn_{1-x}Ge_xS_4$ nanoparticles

The hydrothermal process used for the synthesis of $Cu_2ZnSn_{1-x}Ge_xS_4$ (CZTGS) nanoparticles was adopted from previous works [44,45]. The synthesis process included the preparation of two solutions: (i) a solution with all the cation precursors in 10 mL of DI water, and (ii) a solution of sublimed sulfur in 10 mL of ethylenediamine. In a typical synthesis process, the contents of copper acetate, zinc acetate, and sulfur were fixed at 4 mmol, 2 mmol, and 12 mmol, respectively. As the $GeCl_4$ precursor is highly reactive to humidity, a $GeCl_4$-acetone mixture of 1:31 M ratio was prepared in a glove box under Ar atmosphere and magnetic stirring (6 h), to utilize as a germanium precursor. For preparing the nanostructures with different Ge contents, the $GeCl_4$-acetone mixture precursor and $SnCl_4$ precursor in the reaction mixtures were adjusted to make the nominal Ge mol fractions in the reaction mixture x = Ge/(Sn + Ge) = 0.0, 0.15, 0.30, 0.40, 0.60 and 0.70. The two homogenous solutions were mixed and transferred to a 30 mL Teflon container. The Teflon container was capped and placed inside a stainless-steel autoclave. The sealed autoclave was placed inside a Lindberg Blue gravity furnace and heated to 200 °C (at 3 °C/min). After 24 h of heating, the reactor was naturally cooled down to room temperature. The generated solid product was separated and washed several times with acetone under centrifugation (7000 rpm, 10 min). Finally, the product was dried at 60 °C for 8 h. Several samples were prepared by changing the molar concentrations of Ge and Sn precursors in the reaction solution, maintaining all the other conditions same.

2.3. Elimination of secondary phases by chemical treatment

To remove the byproducts (secondary phases), the freshly prepared CZTGS samples were washed in a 35 mL glass vial, adapting following procedure. First about 700 mg of the sample was mixed with 90 mL of dilute (10 vol% in DI water) HCl. From the 90 mL mixture, 30 mL was taken into the glass vial, covered with its hermetic screw cap, and heated at 80 °C for 45 min under magnetic stirring. Then, the solid was recovered by centrifugation. The same procedure was followed for the remaining 60 mL of the HCl solution. The recovered material was immersed in 30 mL of aqueous KOH (1 M) solution and shaken for 5 min. Finally, the solid was washed with DI water several times, dried under vacuum, and stored under Ar atmosphere. The chemical treatment process was repeated for two times for the $Cu_2ZnSn_{0.3}Ge_{0.7}S_4$ (x = 0.70) sample.

2.4. Deposition of $Cu_2ZnSn_{1-x}Ge_xS_4$ films

For preparing the films of the as-prepared and chemically processed CZTGS nanoparticles, the nanoparticle inks were prepared by dispersing about 150 mg of each of the samples in 0.9 mL of hexanethiol under magnetic stirring for 16 h. The CZTGS nanoparticle inks were spin coated over well cleaned corning glass substrates (1.5×1.5 cm^2). About 25 μL of the prepared ink was dropped over the glass substrate spinning at 2000 rpm for 30 s. After deposition, the films were heated at 95 °C for 10 min. The deposition process was repeated for another time to obtain the films of about 2 μm thickness.

2.5. Characterization

X-ray diffraction (XRD) patterns of the as prepared and chemically treated CZTGS nanoparticles were recorded in a Panalytical – Empyrean diffractometer using CuKα$_1$ radiation (λ = 1.5406 Å) at room temperature. The spectra were recorded at 0.02°/step in the 2θ range of 20–85°. Elemental composition of the samples was estimated by energy dispersive X-ray spectroscopy (EDS) in a JEOL JSM-7800F scanning electron microscope (SEM) with X-Max spectrometer (Oxford Instruments) attached, operating at 15 KeV. Crystalline and vibrational properties of the nanoparticles were studied further by microRaman spectroscopy using a Horiba Lab Ram HR spectrometer equipped with a 633 nm He-Ne laser and a thermoelectrically cooled charge-coupled device (CCD) detector. For analyzing the morphology and fine-structure, the low- and high-resolution transmission electron microscopic images (TEM and HR-TEM) of the nanostructures were recorded in a JEOL 2100F microscope operating at 200 keV. For TEM and HR-TEM analysis, the samples were dispersed over carbon-coated copper grids by drop-casting their colloidal suspension in ethanol. UV–Vis diffuse reflectance spectra of the samples were recorded in a Cary-5000 spectrophotometer with diffuse reflectance accessory attachment (integrating sphere DRA-CA-30I). Electrical properties of the CZTGS films were evaluated at room temperature by measuring the Hall effect in an Ecopia HMS-3000 system under an applied magnetic field of 0.5 T and sample current of 0.1 mA. For electrical characterizations, silver dot contacts were fabricated on the surface of the films in van der Pauw configuration with a separation of 5.0 mm between them. The electrical measurements were performed over 5 films of each of the samples to obtain the average value of each of the parameters. The thickness of the prepared CZTGS films was estimated in a Bruker Dektak 150 Surface Profilometer.

3. Results and discussion

EDS estimated elemental compositions of the as-synthesized CZTGS nanoparticles are listed in Table 1. As can be noticed, all the samples grew with Cu-poor and Zn-rich stoichiometry (Cu/(Zn + Sn + Ge) ≤ 1 and Zn/(Sn + Ge) ≥ 1), and the Ge mol fractions (Ge/(Sn + Ge) ratios) in them are close to the corresponding nominal mol fractions in the reaction mixtures. While such a Cu-poor and Zn-rich stoichiometry of the nanostructures is ideal for their application in photovoltaic devices, formation of secondary phases such as ZnS, $Cu_{2-x}S$ and Cu_2SnS_3 is expected to occur in them [21,46,47]. To investigate whether the Cu-based secondary phases such as $Cu_{2-x}S$ and Cu_2SnS_3 are formed in the samples, they were analyzed by XRD. The room temperature XRD patterns of the nanoparticles synthesized with different nominal Ge mol fractions are shown in Fig. 1a. XRD patterns of all the samples revealed well-resolved diffraction peaks around 28.70, 33.23, 47.65, 56.41, 69.52, and 76.77° Bragg angles, which correspond to the (112), (200), (220), (312), (400) and (136) lattice planes of CZTS in tetragonal kesterite phase (PDF # 04–017-3032), respectively. As can be seen in Fig. 1a, the positions of main XRD peaks such as (112), (220) and (312) of the nanostructures gradually shifted to higher diffraction angles. Such a higher angle shift of the diffraction peaks for the samples containing Ge is probably due to the substitution of Sn atoms of higher ionic radius (Sn^{4+} = 0.69 Å) [48] by the Ge atoms of smaller ionic radius (Ge^{4+} = 0.39 Å). The shift of diffraction peaks towards higher angles in comparison to their positions in the Ge free (i.e., x = 0.0) sample also indicates the incorporation of Ge in crystallite lattice was successful [49–51]. However, for the samples with x = 0.6 and 0.7, there appeared several diffraction peaks associated to Cu_8GeS_6 ternary phase (PDF # 04-010-4016); intensity of which increased gradually with the increase of x value (x ≥ 0.6). In none of the samples we could detect other Cu-based impurity/secondary phases such as $Cu_{2-x}S$ or Cu_2SnS_3 from the XRD patterns.

The incorporation of Ge^{4+} ions in CuS (covellite) and $Cu_{1.81}S$ (roxbyite) phases has been seen to generate Cu_2GeS_3 and Cu_8GeS_6, respectively [52]. As we obtained Cu_8GeS_6 byproduct, it is highly probable that $Cu_{1.81}S$ intermediate was formed at the beginning of the reaction during the hydrothermal treatment utilized for the synthesis of the CZTGS nanostructures. It should be noted that the oxidation states of Cu ions in CuS and $Cu_{1.81}S$ are +2 and +1, respectively. Although the oxidation state of copper in $Cu(CH_3COO)_2·H_2O$ used as copper precursor

Table 1

EDS estimated elemental composition and cation mole fractions in the $Cu_2ZnSn_{1-x}Ge_xS_4$ nanoparticles before washing with HCl solution.

Sample (x-value)	Cu (at%)	Zn (at%)	Sn (at%)	Ge (at%)	S (at%)	Cu/(Zn + Sn + Ge)	Zn/(Sn + Ge)	Ge/(Sn + Ge)
0.0	26.06	14.10	12.31	–	47.54	0.99 ± 0.02	1.15 ± 0.13	0.0
0.15	26.15	13.45	10.54	1.60	48.27	1.02 ± 0.03	1.11 ± 0.05	0.13 ± 0.02
0.30	27.39	16.34	7.72	3.85	44.71	0.98 ± 0.05	1.41 ± 0.09	0.33 ± 0.03
0.40	26.44	13.68	7.54	4.62	47.72	1.02 ± 0.02	1.13 ± 0.06	0.38 ± 0.01
0.60	27.10	15.64	5.23	6.42	45.61	0.99 ± 0.07	1.34 ± 0.06	0.55 ± 0.04
0.70	27.14	16.93	3.79	8.97	43.17	0.91 ± 0.05	1.33 ± 0.06	0.70 ± 0.01

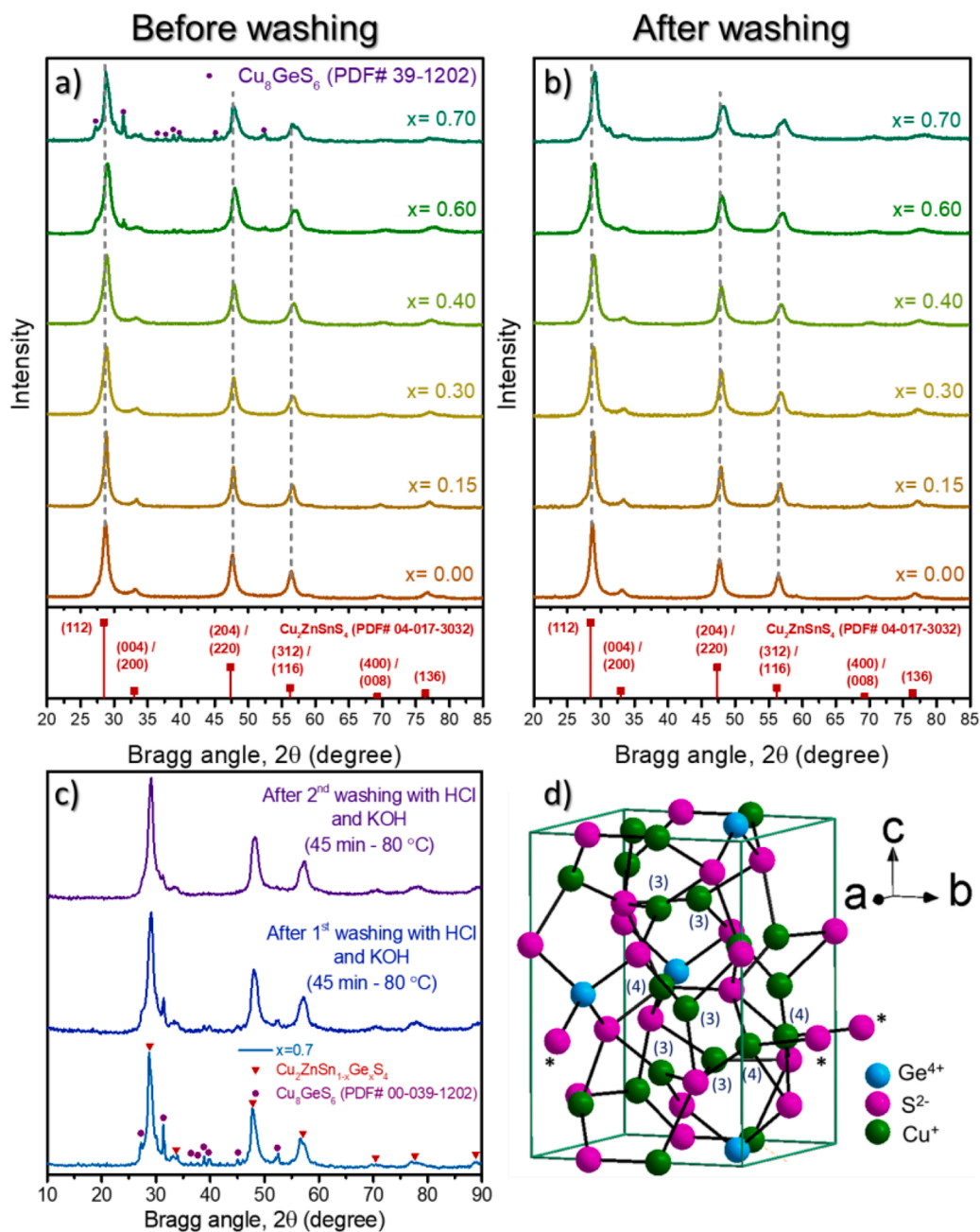**Fig. 1.** XRD patterns of the $Cu_2ZnSn_{1-x}Ge_xS_4$ nanoparticles with different nominal Ge fractions (a) before and (b) after washing them with HCl solution (10%). (c) XRD patterns of the $Cu_2ZnSn_{1-x}Ge_xS_4$ nanoparticles prepared with nominal x = 0.7, before and after 1st and 2nd washing with HCl solution. (d) Schematic presentation of Cu_8GeS_6 structure highlighting that copper ions have coordination number either of three or four, as indicated by the numbers in parenthesis in the scheme. The atoms marked with the asterisk symbols are the ones outside the unit cell.

in the present work was +2, it reduced to +1 by ethylenediamine [53], which facilitated the formation of $Cu_{1.81}S$ intermediate, and finally produce Cu_8GeS_6 phase on reacting with the Ge-precursor. Once the Cu_8GeS_6 phase is formed, it cannot be decomposed even performing the hydrothermal treatment at higher temperature due to its high thermal stability (melting point = 1250 K) [54]. Moreover, the Cu_8GeS_6 phase is reported to be formed around 100 °C, during hydrothermal process [52].

To remove the secondary Cu_8GeS_6 phase, we performed HCl treatment on the $Cu_2ZnSn_{1-x}Ge_xS_4$ samples as described in the previous section. As can be seen in Fig. 1b, the byproduct Cu_8GeS_6 could be

removed successfully through the used wet-chemical treatment. On HCl treatment, the intensity of the diffraction peaks associated with Cu_8GeS_6 phase reduced progressively in the samples prepared with the highest Ge content, without altering the relative intensity of diffraction peaks corresponding to $Cu_2ZnSn_{1-x}Ge_xS_4$ in kesterite phase (Fig. 1(b-c)). While the position of the principal diffraction peaks shifted only marginally towards higher Bragg angles, their full-width at half maximum (FWHM) reduced very slightly after HC-treatment. The results indicate the used HCl treatments has no significant effect on the crystallinity or grain size of the nanoparticles. The Cu_8GeS_6 phase has argyrodite-type structure and most of the compounds with such a structure are superionic conductors due to hopping of Cu^+ ions across the lattice [55–57]. The distance between the neighboring Cu^+ ions in Cu_8GeS_6 is <2.9 Å. Some Cu^+ cations in Cu_8GeS_6 remain bonded to three S^{2-} anions and some remain bonded with four S^{2-} anions (see Fig. 1d). Therefore, the Cu–S bond distances in Cu_8GeS_6 vary in-between 2.219 and 2.590 Å [57,58]. On the contrary, in the kesterite CZTGS lattice, all the Cu^+ cations remain bonded with four S^{2-} anions in regular tetrahedral configuration (Fig. 2c) and the Cu–S bond distance varies in-between 2.26 and 2.29 Å [49]. The longer Cu–S bond distance in Cu_8GeS_6 compared with its distance in CZTGS phase makes the Cu_8GeS_6 phase less stable, which facilitates its etching by diluted HCl [59].

To monitor the effect of Ge incorporation on the lattice structure of the nanostructures, lattice parameters (a = b, c), unit cell volume and gran size were estimated by Rietveld refinement of the XRD patterns of the samples after their chemical treatment, using GSAS-II software (version 4379) [60]. Rietveld refinement outputs of the XRD patterns of the samples are presented in Fig. 2a. For Rietveld refinement, we utilized the EDS estimated composition of the samples, pseudo-Voigt function, the kesterite structure with space group $I\bar{4}$ (PDF# 04–017-3032), and Chebyshev polynomial-based background construction. EDS estimated elemental composition and cation mol fraction in the samples after washing with HCl solution are presented in Table 2. From the EDS estimated compositions of the as-prepared nanostructures, we can observe a gradual increase of Ge content in them with the increase of nominal mol fraction of Ge precursor in the reaction mixture. However, as the Ge/(Ge + Sn) ratio is also dependent on the fraction of Sn substitution by Ge, it is possible that not all the Ge atoms present in the reaction mixture were incorporated into the CZTGS lattice. Those non-participating Ge atoms can produce the ternary Cu_8GeS_6 phase by reacting with the Cu and S precursors in the reaction medium. Fig. 2b

presents the Rietveld refinement extracted structural parameters of the samples after their chemical treatment. As can be observed (Fig. 2b), the values of both the lattice parameters and the unit cell volume decreased almost linearly with the increase of Ge content in the samples. Such linear variations of lattice parameters with x value indicate they follow the Vegard's law [51]:

$$\xi(x) = x\xi_{CZGS} + (1-x)\xi_{CZTS} - \delta x(1-x) \qquad (1)$$

where $\xi(x)$ is the lattice parameter (a or c) of CZTGS, ξ_{CZTS} is the lattice parameter (a or c) of CZTS, ξ_{CZGS} is the lattice parameter of Cu_2ZnGeS_4 (CZGS), δ is the deviation parameter for the lattice constant, and x is the Ge mol fraction in CZTGS. For using in Eq. (1), we considered the lattice parameters of CZTS extracted from the Rietveld analysis of the XRD pattern of the sample without Ge (x = 0.0) and the lattice parameters of CZGS reported in the literature [61]. The best fits to the variations of lattice constant a and c were obtained for the deviation parameter $\delta = 0.01$ and $\delta = 0.1$Å, respectively.

To study the effect of chemical treatment on the size, morphology and crystallinity of the nanostructures, if any, we performed their SEM, TEM and HR-TEM analyses before and after washing with HCl solution. Fig. 3 shows the typical SEM images of the CZTGS nanoparticles with different nominal Ge mol fractions before and after washing with HCl solution. Formation of quasi-spherical particles of nanometer sizes can be observed in the micrographs. As can be observed in Fig. 3, the nanoparticles of all the samples retained their quasi-spherical shape even after washing with HCl solution.

Size distribution histograms performed by measuring the dimensions of individual particles in the HCl-treated samples revealed an average particle size of 12.2 ± 3.6 nm for the sample prepared with 15% of Ge (Fig. 4b). On increasing the amount of Ge in the samples, average size of the nanoparticles reduced marginally (to 11.3 ± 2.5 nm for x = 0.7 sample). Well-resolved atomic planes in the HR-TEM images (Fig. 4(c, f, i and l)) of the HCl-treated nanoparticles indicate their good crystallinity. Intense spots in the fast Fourier transform (FFT) patterns of the selected areas (marked by red squares) of the HR-TEM images clearly indicate the good crystallinity of the nanoparticles. As can be observed in the HR-TEM images presented in the Fig. 4, interplanar distance of the principal lattice (1 1 2) plane of the CZTGS kesterite nanostructures decreases from 3.2 to 2.9 Å with the increase of Ge content. The reduction of average particle size and interplanar distance can be associated to the reduction of the unit cell volume in the crystal lattice on the
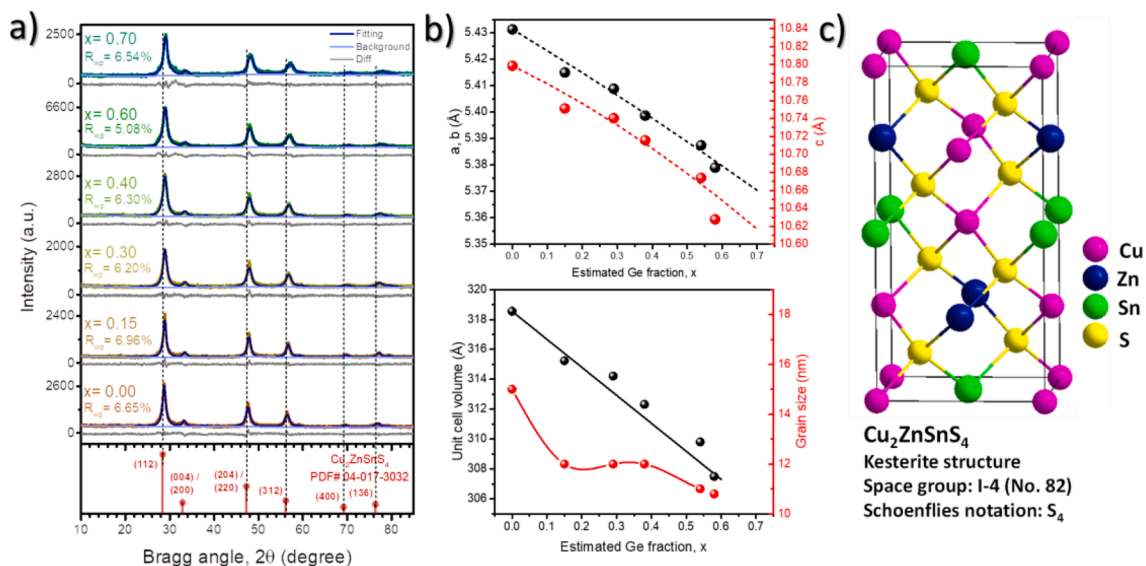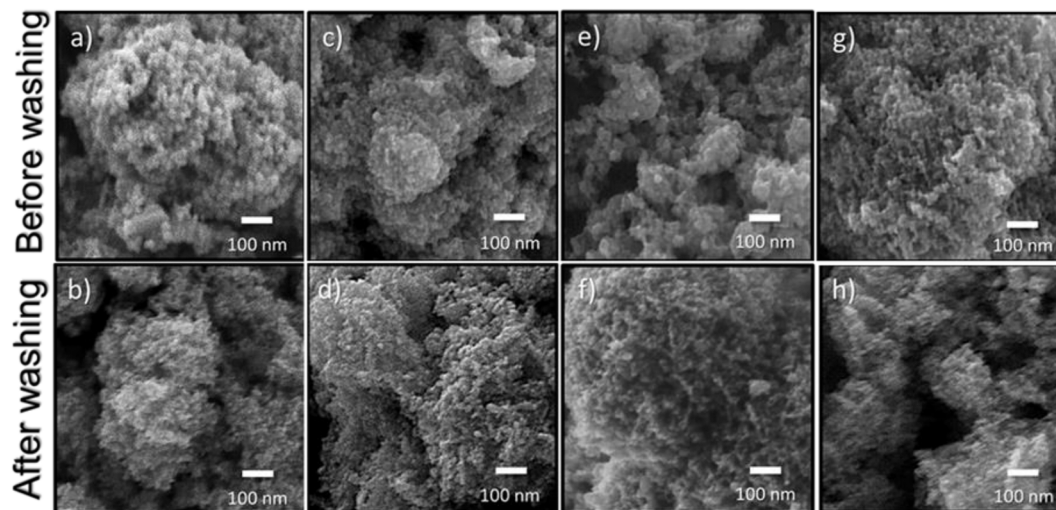

Fig. 2. (a) Rietveld analysis output profiles of the $Cu_2ZnSn_{1-x}Ge_xS_4$ nanoparticles for different Ge fractions (x) after washing them with HCl (10%). (b) Structural parameters extracted from Rietveld analysis of XRD patterns of the nanoparticles after washing. (c) Schematic presentation of the kesterite structure.

Table 2

EDS estimated elemental composition and cation mol fractions in the $Cu_2ZnSn_{1-x}Ge_xS_4$ nanoparticles after washing with HCl solution.

Sample (x-value)	Cu (at%)	Zn (at%)	Sn (at%)	Ge (at%)	S (at%)	Cu/(Zn + Sn + Ge)	Zn/(Sn + Ge)	Ge/(Sn + Ge)
0.0	28.92	10.67	10.62	–	49.79	1.36 ± 0.03	1.02 ± 0.22	0.00
0.15	27.07	10.32	9.38	1.64	51.60	1.27 ± 0.05	0.95 ± 0.20	0.15 ± 0.02
0.30	28.95	10.97	7.55	3.14	49.39	1.34 ± 0.03	1.03 ± 0.05	0.29 ± 0.02
0.40	29.09	10.28	6.86	4.26	49.52	1.36 ± 0.16	0.92 ± 0.02	0.38 ± 0.06
0.60	28.14	12.45	5.08	6.09	48.24	1.20 ± 0.13	1.12 ± 0.18	0.54 ± 0.05
0.70	29.81	9.38	4.48	6.31	50.02	1.48 ± 0.03	0.87 ± 0.04	0.58 ± 0.03

Fig. 3. Typical SEM images of the $Cu_2ZnSn_{1-x}Ge_xS_4$ nanoparticles with different nominal Ge fractions: (a,b) x = 0.0, (c,d) 0.30, (e,f) 0.60, and (g,h) 0.70, before (upper case) and after (lower case) washing them with HCl (10%).

incorporation of Ge, as observed in the structural parameters extracted from Rietveld analysis of XRD patterns of the nanoparticles (Fig. 2b).

As the phase purity and the crystallinity of the nanostructures can be confirmed from their Raman spectra, we performed Raman spectroscopy of the as-prepared and HCl-treated CZTGS nanoparticles at room temperature taking adequate precautions by selecting appropriate objective lenses and filters (neutral density filters) to avoid their oxidation or burning. Room temperature Raman spectra of the CZTGS nanoparticles before and after washing with HCl solution are presented in Fig. 5(a, b), respectively. The Raman spectra of as-prepared and HCl-treated samples revealed an intense dispersion band around 330 cm^{-1}. However, the dispersion band is wide and asymmetric, contains humps at both the sides (lower and higher wavenumber sides) around its maximum. To analyze the features of Raman spectra, the principal Raman band of each of the samples was carefully deconvoluted using Lorentzian curve fitting analysis (Fig. 5(a, b)).

We can see that the principal dispersion band of all the samples (before and after HCl washing) contains three component peaks around 280, 330 and 350 cm^{-1}. According to the literature, the principal dispersion bands of stoichiometric CZTS, the so-called A vibrational modes, are located at 287 and 337 cm^{-1}, which correspond to the rotational and stretching vibration of Sn-S bonds in the SnS_4 tetrahedron of CZTS, respectively. Meanwhile, the component band located around 350 cm^{-1} corresponds to the displacement of cations along the *c*-axis (called as B vibrational mode) [62,63]. However, the A vibrational modes can shift towards lower wavenumbers due to non-stoichiometric composition [64]. In Table 2, we can observe a change in the Zn/(Sn + Ge) and Cu/(Zn + Sn + Ge) ratios for HCl-treated samples in comparison to their values in as-prepared (untreated) samples. The observed change in cation ratios for the HCl-treated samples is probably due to a reduction in Zn content in them (as observed from EDS analysis). The Zn fraction not incorporated into the $Cu_2ZnSn_{1-x}Ge_xS_4$ lattice reacts with sulfur, generating ZnS secondary phase. However, we could not detect

any peak in the XRD patterns of the as-grown nanoparticles associated to the ZnS phase. In fact, the ZnS phase is difficult to be detected in the XRD patterns of the samples as its crystal structure (cubic, $a = 5.41$ Å) is similar to kesterite structure (tetragonal, $a = 5.43$ Å and $c = 10.84$ Å) [20], which produces diffraction peaks at the similar Bragg angles as that of crystalline CZTS. Although Raman spectroscopy with He-Cd laser excitation ($\lambda = 325$ nm) has been utilized to detect the traces of ZnS phase in CZTS films by Fairbrother et al. [42], we could not detect any signal associated to ZnS in our as-prepared nanostructures, probably due to the utilization of He-Ne laser ($\lambda = 633$ nm) for excitation, the energy of which is far below the band gap energy of ZnS ($E_g = 3.6$ eV).

The vibrational modes of the kesterite structure are expected to be sensitive to Ge, incorporated in its lattice. Substitution of Sn by Ge in the kesterite (CZTS) lattice replaces some of the Sn-S bonds by Ge-S bonds, modifying the effective force constant of the cation-anion bonds due to the mass and size differences of the Sn^{4+} and Ge^{4+} ions. Consequently, the positions of Raman dispersion bands are slightly shifted towards higher wavenumber (blue shift) [38,51,65]. The displacement of the principal component band around of 330 cm^{-1} as the function of EDS estimated Ge fraction in the as-prepared and HCl-treated nanostructures are presented in Fig. 5c. As can be noticed, the principal component band in both the as-prepared and HCl-treated samples shifted towards higher wavenumbers with Ge mol fraction, clearly indicating the substitution of Sn by Ge in the kesterite lattice. Moreover, we can observe an offset between the positions of the principal component band of the as-prepared and HCl-treated samples. As revealed from EDS analysis (Table 2), after HCl-treatment, the CZTGS nanoparticles are Cu-rich and Zn-poor (Cu/(Zn + Sn + Ge) ≥ 1 and Zn/(Sn + Ge) ≤ 1), which is the ideal stoichiometry for their application in photovoltaic devices [32]. The small change (≤3 cm^{-1}) in the position of the principal Raman band of the HCl-treated samples is probably attributed to the change in the composition of the nanostructures from Cu-poor to Cu-rich, as has been reported by Valakh et al. [64].
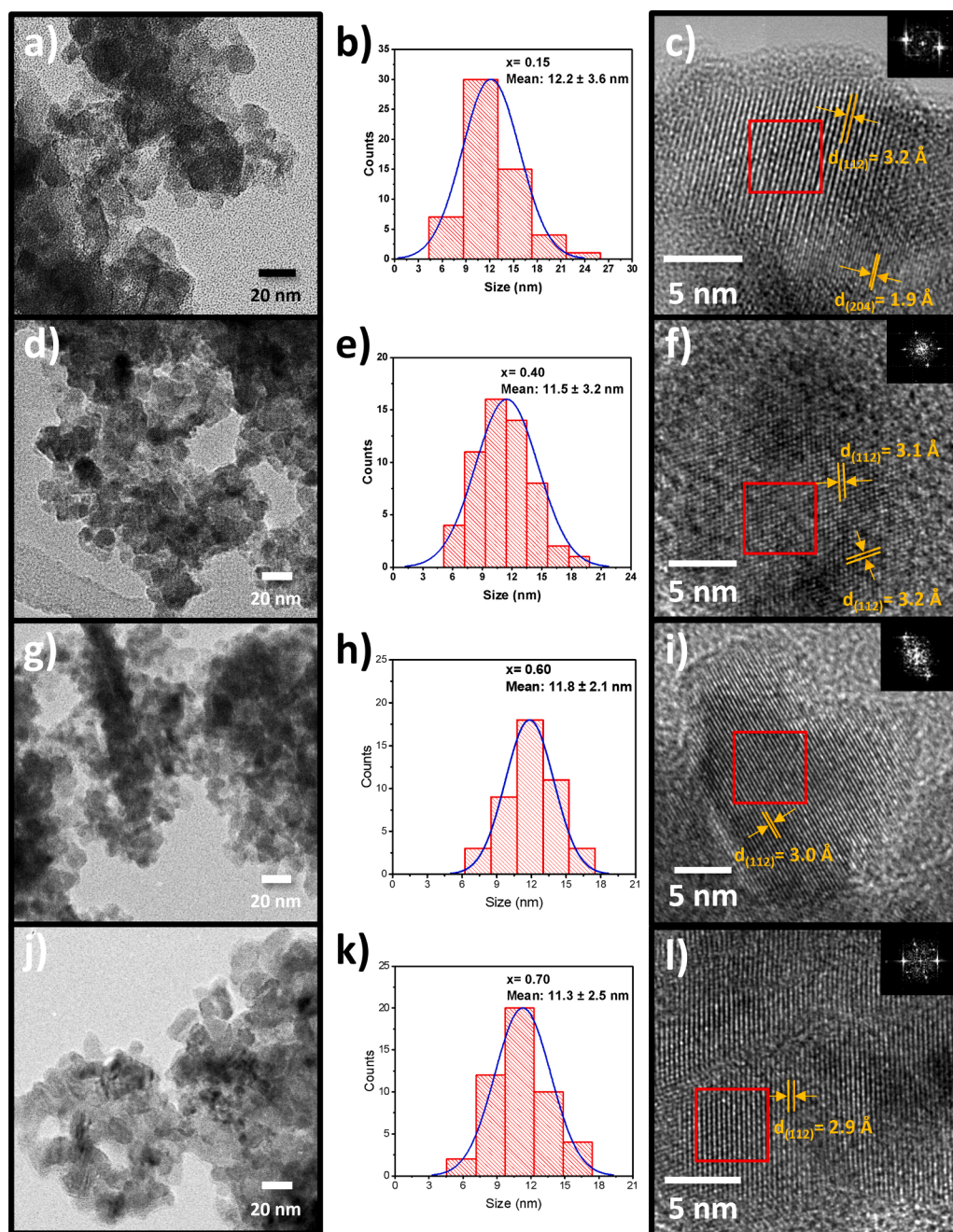
Fig. 4. Typical low- and high-resolution TEM micrographs and corresponding size distribution histograms of the $Cu_2ZnSn_{1-x}Ge_xS_4$ nanoparticles with different nominal Ge fractions: (a-c) x = 0.15, (d-f) x = 0.40, (g-i) x = 0.60, and (j-l) x = 0.70, after washing with HCl solution. Insets in the HR-TEM micrographs correspond to the FFT patterns of the selected areas (red square zones) in each HR-TEM image. (For interpretation of the references to colour in this figure legend, the reader is referred to the web version of this article.)

On the other hand, the full width at half maximum (FWHM) of Raman bands is associated with defect-induced disorder in the kesterite structure (owing to the formation of Cu_{Zn} or Zn_{Cu} antisite defects). The value of FWMH increases with the increase of Cu_{Zn} or Zn_{Cu} antisite defect concentration [64]. As we can see in Fig. 5d, in general, the value of FWHM of the principal Raman band increases with the increase of Ge content in the kesterite lattice. The nanoparticles treated with HCl in this work have Cu-rich and Zn-poor stoichiometry, in which the Cu ions in excess can occupy the Zn sites and produce Cu_{Zn} antisite defects. There occurs also a lattice disorder in the kesterite structure due to the random occupation of Cu and Zn atoms, increasing the concentration of Cu_{Zn} or Zn_{Cu} antisite defects. The disorder in the kesterite lattice also increases due to the substitution of Sn by Ge as observed by several research groups [37,45]. Therefore, the observed increase of FWHM value (Fig. 5d) in the CZTGS nanoparticles prepared in this investigation is probably associated to an increment of disorder in the crystal structure

owing to an increase of Cu_{Zn} antisite defect concentration and the incorporation of Ge at Sn sites of the kesterite lattice. The results obtained from the EDS and Raman spectroscopy analysis of the nanostructures (Table 2 and Fig. 5c, respectively) indicate that under the used synthesis conditions, there exists a maximum limit for the incorporation of Ge in the CZTGS nanoparticles. Incorporation of Ge precursor in the reaction mixture beyond that limit causes the formation of Cu_8GeS_6 secondary phase.

For determining the bandgap energy of the as-prepared and HCl-treated CZTGS nanoparticles, we recorded their diffuse reflectance spectra in 300–920 nm wavelength range (Fig. 6(a, b)). The diffuse reflectance spectra were converted to equivalent absorption spectra using the Kubelka-Munk (K-M) formalism [66]. Fig. 6(c, d) show the K-M plots for the as-prepared and HCl-treated nanoparticles, with linear extrapolations to determine their bandgap energy values. The optical bandgap energy values increased from 1.55 to 1.81 eV and 1.42 to 1.70
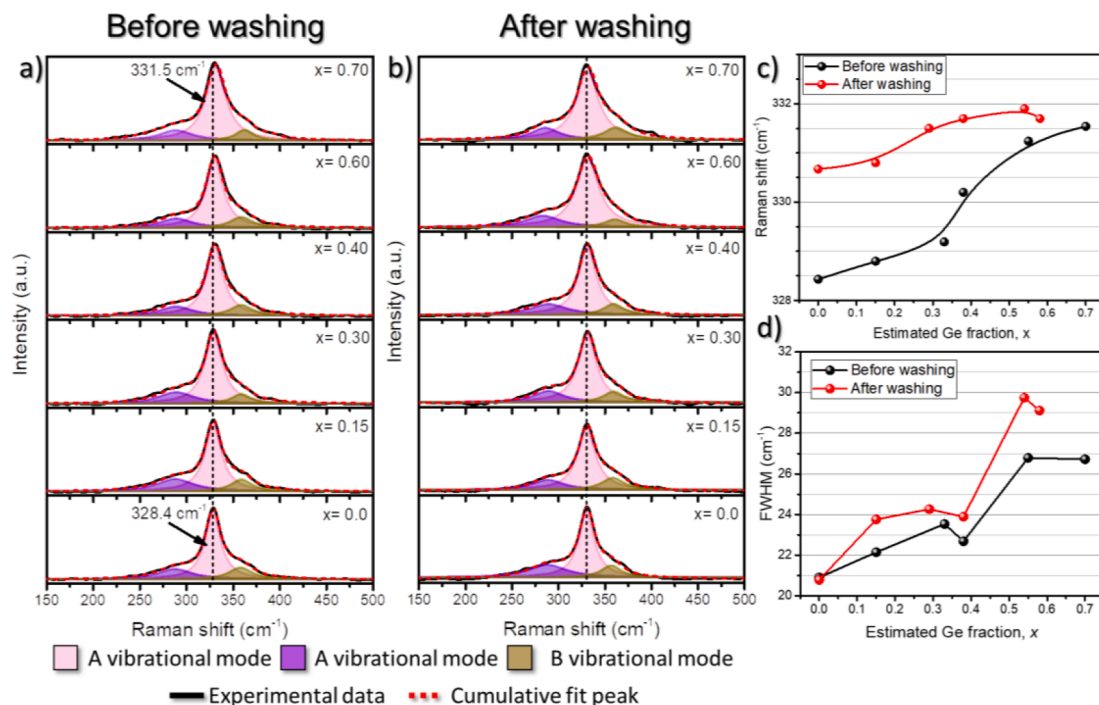
Fig. 5. Room temperature Raman spectra and their deconvolutions for the $Cu_2ZnSn_{1-x}Ge_xS_4$ nanoparticles prepared with different nominal x values: (a) before and (b) after washing with HCl (10%). (c) Variation of peak position and (d) FWHM of the principal component band (around 330 cm^{-1}) with the increase of true (EDS estimated) Ge mol fraction.
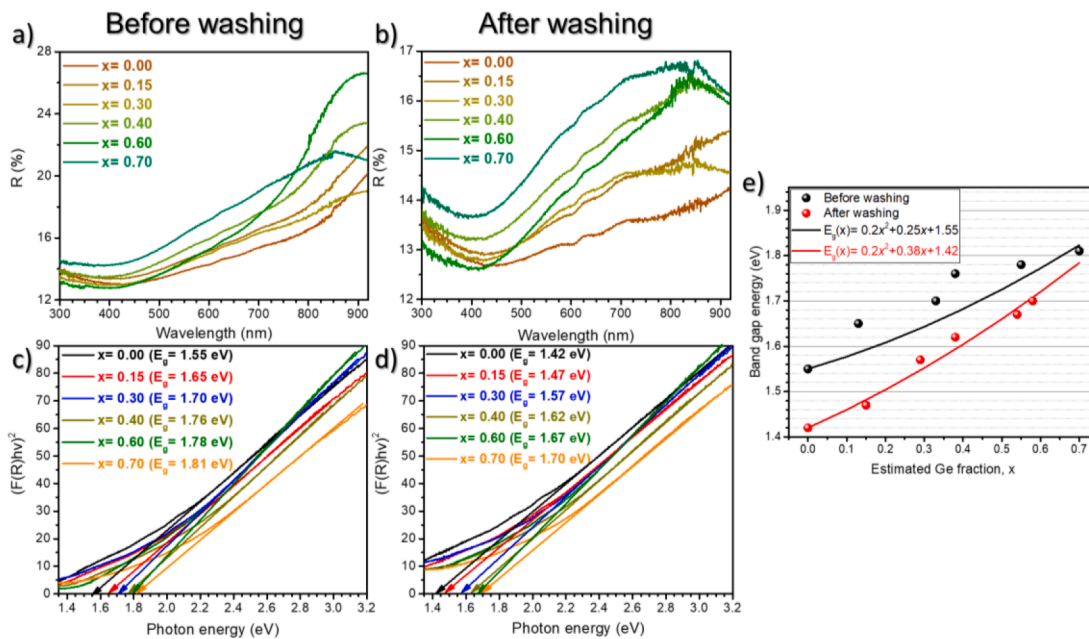

Fig. 6. Diffuse reflectance spectra and Kubelka-Munk plots used to estimate the bandgap energy values of $Cu_2ZnSn_{1-x}Ge_xS_4$ nanoparticles (a,c) before and (b,d) after washing with HCl solution. (e) Variation of bandgap energy with real (EDS estimated) Ge fraction in the nanoparticles. The solid black and red lines correspond to the ideal bandgap energy values according to the Vegard's law. (For interpretation of the references to colour in this figure legend, the reader is referred to the web version of this article.)

eV with the increase of Ge fraction in the samples before and after their HCl treatment, respectively, clearly indicating an increase in bandgap energy due to the substitution of Sn by Ge. The observed increase in the bandgap energy value with increased Ge mol fraction (x) in the kesterite nanoparticles is in good agreement with the results reported by several research groups [38,51,67,68]. The difference in bandgap energy values of a sample containing a certain Ge mol fraction before and after its HCl treatment corresponds to the elimination of impurity phases from it. HCl solution has the capacity of breaking Zn–S bonds in materials of zinc blende structure such as ZnS [42,69]. So, there is a good possibility that HCl attacks $Cu_2ZnSn_{1-x}Ge_xS_4$ kesterite, which has a double zinc blend structure, removing selectively some of the Zn^{2+} ions from the surface of the nanoparticles. To maintain the electroneutrality of the kesterite lattice, equivalent numbers of S^{2-} anions should also be removed from it

or the valence state of its Cu ions should be changed from 1+ to 2+. The removal of Zn^{2+} ions from the surface of kesterite nanoparticles is in accordance with the increment in Cu atomic percentage and reduction of Zn atomic percentage as shown in Table 2. The reduction of the bandgap energy for the HCl-treated samples can be explained in terms of the positions of the valence band maximum (VBM) and conduction band minimum (CBM). In CZTS, the VBM is composed of antibonding Cu-3d and S-3p orbitals, and the CBM is composed of antibonding combinations of Sn-5s and S-3p orbitals [17]. Selective elimination of the Zn^{2+} ions from the surface of CZTGS nanoparticles due on HCl treatment probably promotes the formation of acceptor levels close to the VBM owing to change the oxidation state of Cu from Cu^{1+} to Cu^{2+} [16,70–72], reducing their effective bandgap energy.

The empirical relationship between the bandgap energy value and Ge/(Ge + Sn) ratio in the kesterite can be expressed by the Vegard's relation (**Eq. (2)**) with a correction term, known as bowing parameter (associated to the curvature of the bandgap energies):

$$E_g^{CZTGS}(x) = xE_g^{CZGS} + (1-x)E_g^{CZTS} - bx(1-x) \qquad (2)$$

where E_g^{CZTS} and E_g^{CZGS} are the bandgap energies of CZTS and CZGS respectively, x is the Ge mol fraction in CZTGS and b is the bowing parameter which describes the degree of nonlinearity. The experimentally obtained data for both the untreated and HCl treated samples were found to be best fitted for a bowing constant equal to 0.2 eV, as has also been reported by Mora-Herrera et al. and Chen et al. [37,51]. The small bowing constant implies that the bandgap energy of CZTGS nanostructures increase almost linearly with the increase of Ge mol fraction (x). For calculating bandgap energies of the $Cu_2ZnSn_{1-x}Ge_xS_4$ nanostructures we utilized the experimentally determined bandgap energy values of the CZTS nanoparticles before and after HCl treatment (1.55

and 1.42 eV) and the literature reported bandgap energy value of pure CZGS (2.0 eV) [38,51]. The solid black and red colored curves in Fig. 6e show the calculated bandgap energy variations for the CZTGS nanoparticles with different x values before and after their HCl treatment. As can be noticed, the experimentally determined bandgap energy values of the chemically treated samples are very close to their empirical values. However, the experimentally determined bandgap energy values of the as-prepared (untreated) samples deviated significantly from their empirical ones due to the presence of secondary phases Cu_8GeS_6 and ZnS.

As the transport properties of the kesterite semiconductors, such as their electrical resistivity (ρ), carrier concentration (p), and carrier mobility (μ), are important parameters which define their application in optoelectronic devices such as PSCs, we performed room temperature conductivity and Hall measurements on the spin-coated films of the as-prepared and chemically treated nanoparticles. Average thickness of the as-prepared and chemically treated films utilized for electrical characterizations were 2.34 ± 0.44 and 2.21 ± 0.66 μm, respectively. The arrangement of the silver contacts over CZTGS films utilized to measure the resistivity and Hall effect is present in Fig. 7a.

As can be seen in Fig. 7b, electrical conductivity of the kesterite films prepared with as-prepared nanoparticles did not vary substantially with the increase of nominal mol fraction of Ge. However, the films prepared with chemically treated nanoparticles revealed significant increase in conductivity, for all the Ge fraction values (Fig. 7b). All the samples revealed positive Hall voltage, indicating their p-type electrical conductivity at room temperature. In fact, CZTS is intrinsically a p-type semiconductor due to the presence of Cu_{Zn} antisite and Cu-vacancy defects [16,70–72]. As can be seen in Fig. 7c, all the films prepared with untreated nanoparticles revealed high carrier concentration, which
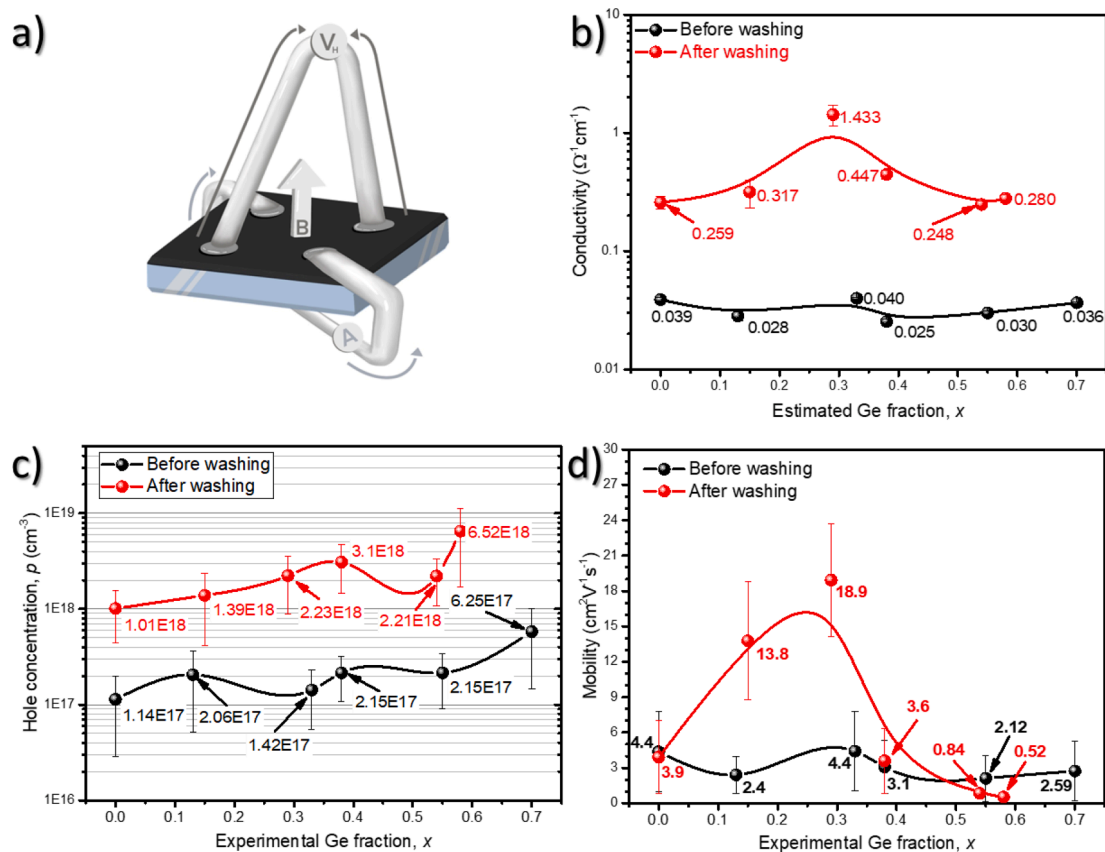

Fig. 7. (a) Schematic representation of the arrangement of the silver dot contacts over the CZTGS films used to measure resistivity and Hall voltage (V_H). The arrow B shows the direction of applied magnetic field. Variations of (b) electrical conductivity (σ), (c) carrier concentration (p) and (d) carrier mobility (μ), in the $Cu_2ZnSn_{1-x}Ge_xS_4$ films prepared with as-prepared and HCl-treated.

increased from 1.14×10^{17} to 6.25×10^{17} cm^{-3} with the increase of Ge mol fraction (x) from 0.0 to 0.7. Such an increase in hole concentration in the films can be associated to an increase in Cu$_{Zn}$ antisite defects in the nanostructures with the increase of Ge mol fraction. In fact, the increase of Cu$_{Zn}$ antisite defects with increased x value was also noticed in the Raman spectra of the samples (Fig. 5). The Cu$_{Zn}$ antisite defects form an acceptor level in the bandgap of kesterite close to its valence band and contribute to the concentration of the charge carriers in the kesterite [16,70–72]. Therefore, the observed increase in carrier concentration of the CZTGS films with increased Ge mol fraction is probably due to higher concentration of Cu$_{Zn}$ antisite defects in them. Besides, we can observe a substantial increase in carrier concentration by about one order of magnitude (from $\sim10^{17}$ to $\sim10^{18}$ cm^{-3}) for the films prepared with HCl-treated kesterite nanoparticles. This increase is due to higher concentration of Cu$_{Zn}$ antisite defects in the films prepared with HCl-treated kesterite nanoparticles. The increment in Cu$_{Zn}$ antisite defects is in accordance with the results observed in the diffuse reflectance spectroscopy of the samples.

Electrical conductivity of the films fabricated using as-prepared nanoparticles remained almost unchanged with the increase of Ge content. However, the conductivity increased noticeably after washing the nanoparticles with HCl, probably due to the removal of secondary phases from them. It should be recalled that we could not detect the presence of secondary phases such as Cu$_{2-x}$S or Cu$_2$SnS$_3$ in the XRD or Raman spectra either of the as-prepared or HCl-treated samples. Therefore, the observed change in conductivity must be associated to ZnS in the nanostructures, which was eliminated by HCl treatment. On the other hand, the mobility of the charge carrier in the films prepared using as-prepared nanoparticles did not vary significantly with the variation of nominal Ge fraction (Fig. 7**d**). The observed non-variant nature of carrier mobility in the samples probably due to the presence of ZnS phase, which is an insulator material. Therefore, we expected an increase in carrier mobility for the films prepared using HCl-treated nanostructures. However, as can be observed in Fig. 7**d**, the HCl treatment enhanced the carrier mobility only up to x $\sim$ 0.3. For higher Ge content (x $\geq$ 0.4) kesterite films, the mobility decreased from 3.6 to 0.52 cm^{2}V^{-1}s^{-1}. The observed reduction in carrier mobility for higher Ge content films prepared with HCl-treated nanoparticles is probably due to the removal of Cu$_8$GeS$_6$ phase, which has been reported as a p-type semiconductor with high hole mobility (~16 cm^{2}V^{-1}s^{-1}) [73]. The Cu$_8$GeS$_6$ formed in the samples has a large particle size, as evidenced by the narrow diffraction peak at around $2\theta = 43.73^\circ$ in the XRD spectra of the CZTGS films of higher Ge content (Fig. 1**a**), which enhances the carrier mobility. Removal or etching out of those bigger Cu$_8$GeS$_6$ grains from the samples causes a reduction in the hole mobility for the films prepared with HCl-treated CZTGS nanoparticles. On the other hand, the reduction of hole mobility for higher x-value (x > 0.3) samples can also be due to their very high carrier concentration, which induces carrier scattering (hole-lattice) in the sample, even at room temperature.

4. Conclusions

In summary, we demonstrated the fabrication of quasi-spherical Cu$_2$ZnSn$_{1-x}$Ge$_x$S$_4$ nanoparticles of about 11 nm average size with predominant kesterite phase through a low-temperature hydrothermal process. Incorporation of Ge in the kesterite nanostructures induces the formation of secondary phases such as ZnS and Cu$_8$GeS$_6$, depending on the mole fraction of Ge used to prepare them. The secondary phases formed in the nanoparticles could be completely removed by treating them with dilute (10%) HCl solution at 80 °C. The HCl treatment does not affect the kesterite structure, neither it affects the size and morphology of the nanoparticles. Incorporation of Ge enhances the concentration of Cu$_{Zn}$ antisite defect in the kesterite lattice, enhances the hole concentration in the kesterite nanoparticles. Transport behaviors of the CZTGS films prepared using HCl-treated kesterite nanoparticles indicate that they are promising candidates for utilization as HTLs. The results presented in this study are useful for developing CZTGS-based photovoltaic devices with high photoconversion efficiency.

CRediT authorship contribution statement

Francisco Enrique Cancino-Gordillo: Methodology, Formal analysis, Investigation, Visualization, Writing - original draft, Writing - review & editing. **José-Luis Ortiz-Quiñonez:** Investigation, Writing-review & editing, Validation, Formal analysis. **Mou Pal:** Writing-review & editing, Validation. **Rutilo Silva González:** Formal analysis, Validation, Visualization. **Umapada Pal:** Conceptualization, Methodology, Supervision, Funding acquisition, Project administration, Resources, Writing - original draft, Writing - review & editing.

Declaration of Competing Interest

The authors declare that they have no known competing financial interests or personal relationships that could have appeared to influence the work reported in this paper.

Data availability

Data will be made available on request.

Acknowledgments

References

[1] M. Grossberg, J. Krustok, C.J. Hages, D.M. Bishop, O. Gunawan, R. Scheer, S. M. Lyam, H. Hempel, S. Levcenco, T. Unold, The electrical and optical properties of kesterites, J. Phys. Energy. 1 (2019), 044002, https://doi.org/10.1088/2515-7655/ab29a0.

[2] K. Pal, P. Singh, A. Bhaduri, K.B. Thapa, Current challenges and future prospects for a highly efficient (20%) kesterite CZTS solar cell: A review, Sol. Energy Mater. Sol. Cells 196 (2019) 138–156, https://doi.org/10.1016/j.solmat.2019.03.001.

[3] C. Yan, J. Huang, K. Sun, S. Johnston, Y. Zhang, H. Sun, A. Pu, M. He, F. Liu, K. Eder, L. Yang, J.M. Cairney, N.J. Ekins-Daukes, Z. Hameiri, J.A. Stride, S. Chen, M.A. Green, X. Hao, Cu$_2$ZnSnS$_4$ solar cells with over 10% power conversion efficiency enabled by heterojunction heat treatment, Nat. Energy 3 (2018) 764–772, https://doi.org/10.1038/s41560-018-0206-0.

[4] W. Wang, M.T. Winkler, O. Gunawan, T. Gokmen, T.K. Todorov, Y. Zhu, D.B. Mitzi, Device Characteristics of CZTSSe Thin-Film Solar Cells with 12.6% Efficiency, Adv. Energy Mater. 4 (2014) 1301465, https://doi.org/10.1002/aenm.201301465.

[5] M.A. Green, E.D. Dunlop, J. Hohl-Ebinger, M. Yoshita, N. Kopidakis, X. Hao, Solar cell efficiency tables (Version 58), Prog. Photovoltaics Res. Appl. 29 (2021) 657–667, https://doi.org/10.1002/pip.3444.

[6] M.H. Sharif, T. Enkhbat, E. Enkhbayar, J. Kim, Control of Defect States of Kesterite Solar Cells to Achieve More Than 11% Power Conversion Efficiency, ACS Appl. Energy Mater. 3 (2020) 8500–8508, https://doi.org/10.1021/acsaem.0c01141.

[7] P. Liu, W. Wang, S. Liu, H. Yang, Z. Shao, Fundamental Understanding of Photocurrent Hysteresis in Perovskite Solar Cells, Adv. Energy Mater. 9 (2019) 1803017, https://doi.org/10.1002/aenm.201803017.

[8] A.M. Elseman, S. Sajid, A.E. Shalan, S.A. Mohamed, M.M. Rashad, Recent progress concerning inorganic hole transport layers for efficient perovskite solar cells, Appl. Phys. A Mater. Sci. Process. 125 (2019), https://doi.org/10.1007/s00339-019-2766-7.

[9] I.M. Peters, T. Buonassisi, Energy Yield Limits for Single-Junction Solar Cells, Joule 2 (2018) 1160–1170, https://doi.org/10.1016/j.joule.2018.03.009.

[10] M.M.S. Sanad, A.M. Elseman, M.M. Elsenety, B.A. Elsayed, Facile synthesis of sulfide-based chalcogenide as hole-transporting materials for cost-effective efficient perovskite solar cells, J. Mater. Sci. Mater. Electron. 30 (2019) 6868–6875, https://doi.org/10.1007/s10854-019-01001-z.

[11] U. Syafiq, N. Ataollahi, P. Scardi, Progress in CZTS as hole transport layer in perovskite solar cell, Sol. Energy. 196 (2020) 399–408, https://doi.org/10.1016/j.solener.2019.12.016.

[12] Q. Wu, C. Xue, Y. Li, P. Zhou, W. Liu, J. Zhu, S. Dai, C. Zhu, S. Yang, Kesterite Cu$_2$ZnSnS$_4$ as a Low-Cost Inorganic Hole-Transporting Material for High-Efficiency Perovskite Solar Cells, ACS Appl. Mater. Interfaces 7 (2015) 28466–28473, https://doi.org/10.1021/acsami.5b09572.

[13] M. Yuan, X. Zhang, J. Kong, W. Zhou, Z. Zhou, Q. Tian, Y. Meng, S. Wu, D. Kou, Controlling the Band Gap to Improve Open-Circuit Voltage in Metal Chalcogenide

based Perovskite Solar Cells, Electrochim. Acta 215 (2016) 374–379, https://doi.org/10.1016/j.electacta.2016.08.130.

[14] M. Kumar, A. Dubey, N. Adhikari, S. Venkatesan, Q. Qiao, Strategic review of secondary phases, defects and defect-complexes in kesterite CZTS–Se solar cells, Energy Environ. Sci. 8 (2015) 3134–3159, https://doi.org/10.1039/C5EE02153G.

[15] S. Chen, L.-W. Wang, A. Walsh, X.G. Gong, S.-H. Wei, Abundance of $Cu_{Zn} + Sn_{Zn}$ and $2Cu_{Zn} + Sn_{Zn}$ defect clusters in kesterite solar cells, Appl. Phys. Lett. 101 (2012), 223901, https://doi.org/10.1063/1.4768215.

[16] D. Han, Y.Y. Sun, J. Bang, Y.Y. Zhang, H.-B. Sun, X.-B. Li, S.B. Zhang, Deep electron traps and origin of p-type conductivity in the earth-abundant solar-cell material Cu_2ZnSnS_4, Phys. Rev. B 87 (2013), 155206, https://doi.org/10.1103/PhysRevB.87.155206.

[17] S. Chen, A. Walsh, X.-G. Gong, S.-H. Wei, Classification of Lattice Defects in the Kesterite Cu_2ZnSnS_4 and $Cu_2ZnSnSe_4$ Earth-Abundant Solar Cell Absorbers, Adv. Mater. 25 (2013) 1522–1539, https://doi.org/10.1002/adma.201203146.

[18] K. Biswas, S. Lany, A. Zunger, The electronic consequences of multivalent elements in inorganic solar absorbers: Multivalency of Sn in Cu_2ZnSnS_4, Appl. Phys. Lett. 96 (2010), 201902, https://doi.org/10.1063/1.3427433.

[19] H. Du, F. Yan, M. Young, B. To, C.-S. Jiang, P. Dippo, D. Kuciauskas, Z. Chi, E. A. Lund, C. Hancock, W.M. Hlaing OO, M.A. Scarpulla, G. Teeter, Investigation of combinatorial coevaporated thin film Cu_2ZnSnS_4. I. Temperature effect, crystalline phases, morphology, and photoluminescence, J. Appl. Phys. 115 (2014), 173502, https://doi.org/10.1063/1.4871664.

[20] G. Altamura, J. Vidal, Impact of Minor Phases on the Performances of CZTSSe Thin-Film Solar Cells, Chem. Mater. 28 (2016) 3540–3563, https://doi.org/10.1021/acs.chemmater.6b00069.

[21] W.-S. Liu, S.-Y. Chen, C.-S. Huang, M.-Y. Lee, H.-C. Kuo, Investigation of Zn/Sn ratio for improving the material quality of CZTS thin films with the reduction of $Cu_{2-x}S$ secondary phase, J. Alloys Compd. 853 (2021), 157237, https://doi.org/10.1016/j.jallcom.2020.157237.

[22] J. Xu, J. Yang, S. Jiang, S. Shang, Secondary phases and disorder degree investigation of Cu_2ZnSnS_4 films, Ceram. Int. 47 (2021) 4135–4142, https://doi.org/10.1016/j.ceramint.2020.09.290.

[23] I.S. Babichuk, M.O. Semenenko, S. Golovynskyi, R. Caballero, O.I. Datsenko, I. V. Babichuk, J. Li, G. Xu, R. Qiu, C. Huang, R. Hu, I. Golovynska, V. Ganus, B. Li, J. Qu, M. Leon, Control of secondary phases and disorder degree in Cu_2ZnSnS_4 films by sulfurization at varied subatmospheric pressures, Sol. Energy Mater. Sol. Cells. 200 (2019) 109915, https://doi.org/10.1016/j.solmat.2019.109915.

[24] M.G. Gang, V.C. Karade, M.P. Suryawanshi, H. Yoo, M. He, X. Hao, I.J. Lee, B. H. Lee, S.W. Shin, J.H. Kim, A Facile Process for Partial Ag Substitution in Kesterite $Cu_2ZnSn(S, Se)_4$ Solar Cells Enabling a Device Efficiency of over 12%, ACS Appl. Mater. Interfaces 13 (2021) 3959–3968, https://doi.org/10.1021/acsami.0c19373.

[25] C. Ma, H. Guo, K. Zhang, N. Yuan, J. Ding, Fabrication of p-type kesterite Ag_2ZnSnS_4 thin films with a high hole mobility, Mater. Lett. 186 (2017) 390–393, https://doi.org/10.1016/j.matlet.2016.10.013.

[26] H. Guo, C. Ma, K. Zhang, X. Jia, Y. Li, N. Yuan, J. Ding, The fabrication of Cd-free Cu_2ZnSnS_4-Ag_2ZnSnS_4 heterojunction photovoltaic devices, Sol. Energy Mater. Sol. Cells 178 (2018) 146–153, https://doi.org/10.1016/j.solmat.2018.01.022.

[27] S. Hadke, S. Levcenko, G. Sai Gautam, C.J. Hages, J.A. Márquez, V. Izquierdo-Roca, E.A. Carter, T. Unold, L.H. Wong, Suppressed Deep Traps and Bandgap Fluctuations in Cu_2CdSnS_4 Solar Cells with ≈8% Efficiency, Adv. Energy Mater. 9 (2019) 1902509, https://doi.org/10.1002/aenm.201902509.

[28] M. Cao, L. Li, W.Z. Fan, X.Y. Liu, Y. Sun, Y. Shen, Quaternary Cu_2CdSnS_4 nanoparticles synthesized by a simple solvothermal method, Chem. Phys. Lett. 534 (2012) 34–37, https://doi.org/10.1016/j.cplett.2012.03.016.

[29] C.J. Hages, S. Levcenco, C.K. Miskin, J.H. Alsmeier, D. Abou-Ras, R.G. Wilks, M. Bär, T. Unold, R. Agrawal, Improved performance of Ge-alloyed CZTGeSSe thin-film solar cells through control of elemental losses, Prog. Photovoltaics Res. Appl. 23 (2015) 376–384, https://doi.org/10.1002/pip.2442.

[30] S. Giraldo, M. Neuschitzer, T. Thersleff, S. López-Marino, Y. Sánchez, H. Xie, M. Colina, M. Placidi, P. Pistor, V. Izquierdo-Roca, K. Leifer, A. Pérez-Rodríguez, E. Saucedo, Large Efficiency Improvement in $Cu_2ZnSnSe_4$ Solar Cells by Introducing a Superficial Ge Nanolayer, Adv. Energy Mater. 5 (2015) 1501070, https://doi.org/10.1002/aenm.201501070.

[31] S. Kim, K.M. Kim, H. Tampo, H. Shibata, S. Niki, Improvement of voltage deficit of Ge-incorporated kesterite solar cell with 12.3% conversion efficiency, Appl. Phys. Express. 9 (2016), 102301, https://doi.org/10.7567/APEX.9.102301.

[32] K.-S. Lim, S.-M. Yu, S. Seo, H. Shin, T.-S. Oh, J.-B. Yoo, Incorporation of Ge in Cu_2ZnSnS_4 thin film in a Zn-poor composition range, Mater. Sci. Semicond. Process. 89 (2019) 194–200, https://doi.org/10.1016/j.mssp.2018.09.020.

[33] L. Choubrac, M. Bär, X. Kozina, R. Félix, R.G. Wilks, G. Brammertz, S. Levcenko, L. Arzel, N. Barreau, S. Harel, M. Meuris, B. Vermang, Sn Substitution by Ge: Strategies to Overcome the Open-Circuit Voltage Deficit of Kesterite Solar Cells, ACS Appl. Energy Mater. 3 (2020) 5830–5839, https://doi.org/10.1021/acsaem.0c00763.

[34] J. Li, D. Wang, X. Li, Y. Zeng, Y. Zhang, Cation Substitution in Earth-Abundant Kesterite Photovoltaic Materials, Adv. Sci. 5 (2018), https://doi.org/10.1002/advs.201700744.

[35] M. Ritzer, S. Schönherr, P. Schöppe, W. Wisniewski, S. Giraldo, G. Gurieva, A. Johannes, C.T. Plass, K. Ritter, G. Martínez-Criado, S. Schorr, E. Saucedo, C. Ronning, C.S. Schnohr, On the Germanium Incorporation in $Cu_2ZnSnSe_4$ Kesterite Solar Cells Boosting Their Efficiency, ACS Appl. Energy Mater. 3 (2020) 558–564, https://doi.org/10.1021/acsaem.9b01784.

[36] M. Neuschitzer, M.E. Rodriguez, M. Guc, J.A. Marquez, S. Giraldo, I. Forbes, A. Perez-Rodriguez, E. Saucedo, Revealing the beneficial effects of Ge doping on

[37] $Cu_2ZnSnSe_4$ thin film solar cells, J. Mater. Chem. A 6 (2018) 11759–11772, https://doi.org/10.1039/C8TA02551G.

[37] D. Mora-Herrera, M. Pal, F. Paraguay-Delgado, Facile solvothermal synthesis of $Cu_2ZnSn_{1-x}Ge_xS_4$ nanocrystals: Effect of Ge content on optical and electrical properties, Mater. Chem. Phys. 257 (2021), 123764, https://doi.org/10.1016/j.matchemphys.2020.123764.

[38] X. Lv, C. Zhu, H. Hao, R. Liu, Y. Wang, J. Wang, Improving the performance of low-cost water-based solution-synthesised $Cu_2ZnSn_{1-x}Ge_x(S, Se)_4$ absorber thin films by germanium doping, Ceram. Int. 46 (2020) 25638–25645, https://doi.org/10.1016/j.ceramint.2020.07.039.

[39] M. Neuschitzer, J. Marquez, S. Giraldo, M. Dimitrievska, M. Placidi, I. Forbes, V. Izquierdo-Roca, A. Pérez-Rodriguez, E. Saucedo, V_{oc} Boosting and Grain Growth Enhancing Ge-Doping Strategy for $Cu_2ZnSnSe_4$ Photovoltaic Absorbers, J. Phys. Chem. C 120 (2016) 9661–9670, https://doi.org/10.1021/acs.jpcc.6b02315.

[40] A.D. Collord, H.W. Hillhouse, Germanium Alloyed Kesterite Solar Cells with Low Voltage Deficits, Chem. Mater. 28 (2016) 2067–2073, https://doi.org/10.1021/acs.chemmater.5b04806.

[41] M. Buffière, G. Brammertz, S. Sahayaraj, M. Batuk, S. Khelifi, D. Mangin, A.-A. El Mel, L. Arzel, J. Hadermann, M. Meuris, J. Poortmans, KCN Chemical Etch for Interface Engineering in $Cu_2ZnSnSe_4$ Solar Cells, ACS Appl. Mater. Interfaces 7 (2015) 14690–14698, https://doi.org/10.1021/acsami.5b02122.

[42] A. Fairbrother, E. García-Hemme, V. Izquierdo-Roca, X. Fontané, F.A. Pulgarín-Agudelo, O. Vigil-Galán, A. Pérez-Rodriguez, E. Saucedo, Development of a Selective Chemical Etch To Improve the Conversion Efficiency of Zn-Rich Cu_2ZnSnS_4 Solar Cells, J. Am. Chem. Soc. 134 (2012) 8018–8021, https://doi.org/10.1021/ja301373e.

[43] M. Mousel, A. Redinger, R. Djemour, M. Arasimowicz, N. Valle, P. Dale, S. Siebentritt, HCl and Br_2-MeOH etching of $Cu_2ZnSnSe_4$ polycrystalline absorbers, Thin Solid Films 535 (2013) 83–87, https://doi.org/10.1016/j.tsf.2012.12.095.

[44] X. Peng, S. Zhang, Y. Xiang, Solvothermal synthesis of $Cu_2Zn(Sn_{1-x}Ge_x)S_4$ and $Cu_2(Sn_{1-x}Ge_x)S_3$ nanoparticles with tunable band gap energies, J. Alloys Compd. 640 (2015) 75–81, https://doi.org/10.1016/j.jallcom.2015.03.248.

[45] F.E. Cancino-Gordillo, J.V. Cab, U. Pal, Structure and transport behavior of hydrothermally grown phase pure $Cu_2ZnSn_{1-x}Ge_xS_4$ (x = 0.0, 0.3) nanoparticles, Appl. Surf. Sci. 571 (2022), 151261, https://doi.org/10.1016/j.apsusc.2021.151261.

[46] A. Fairbrother, X. Fontané, V. Izquierdo-Roca, M. Espíndola-Rodríguez, S. López-Marino, M. Placidi, L. Calvo-Barrio, A. Pérez-Rodriguez, E. Saucedo, On the formation mechanisms of Zn-rich Cu_2ZnSnS_4 films prepared by sulfurization of metallic stacks, Sol. Energy Mater. Sol. Cells 112 (2013) 97–105, https://doi.org/10.1016/j.solmat.2013.01.015.

[47] A. Fairbrother, X. Fontané, V. Izquierdo-Roca, M. Placidi, D. Sylla, M. Espindola-Rodriguez, S. López-Mariño, F.A. Pulgarín, O. Vigil-Galán, A. Pérez-Rodriguez, E. Saucedo, Secondary phase formation in Zn-rich Cu_2ZnSnS_4-based solar cells annealed in low pressure and temperature conditions, Prog. Photovoltaics Res. Appl. 22 (2014) 479–487, https://doi.org/10.1002/pip.2473.

[48] R.D. Shannon, Revised effective ionic radii and systematic studies of interatomic distances in halides and chalcogenides, Acta Crystallogr. Sect. A 32 (1976) 751–767, https://doi.org/10.1107/S0567739476001551.

[49] M. Morihama, F. Gao, T. Maeda, T. Wada, Crystallographic and optical properties of $Cu_2Zn(Sn_{1-x}Ge_x)Se_4$ solid solution, Jpn. J. Appl. Phys. 53 (2014) 04ER09, https://doi.org/10.7567/JJAP.53.04ER09.

[50] J. Chen, W. Li, C. Yan, S. Huang, X. Hao, Studies of compositional dependent $Cu_2Zn(Ge_xSn_{1-x})S_4$ thin films prepared by sulfurizing sputtered metallic precursors, J. Alloys Compd. 621 (2015) 154–161, https://doi.org/10.1016/j.jallcom.2014.09.097.

[51] G. Chen, W. Wang, S. Chen, Z. Whang, Z. Huang, B. Zhang, X. Kong, Bandgap engineering of $Cu_2ZnSn_{1-x}Ge_xS(e)_4$ by adjusting Sn-Ge ratios for almost full solar spectrum absorption, J. Alloys Compd. 718 (2017) 236–245, https://doi.org/10.1016/j.jallcom.2017.05.150.

[52] M.D. Regulacio, S.Y. Tee, S.H. Lim, Z. Zhang, M.-Y. Han, Selective formation of ternary Cu–Ge–S nanostructures in solution, CrystEngComm. 20 (2018) 6803–6810, https://doi.org/10.1039/C8CE01443D.

[53] B. Li, Y. Xie, J. Huang, Y. Qian, Synthesis by a Solvothermal Route and Characterization of CuInSe$_2$ Nanowhiskers and Nanoparticles, Adv. Mater. 11 (1999) 1456–1459, https://doi.org/10.1002/(SICI)1521-4095(199912)11:17<1456::AID-ADMA1456>3.0.CO;2-3.

[54] I.J. Alverdiyev, Z.S. Aliev, S.M. Bagheri, L.F. Mashadiyeva, Y.A. Yusibov, M. B. Babanly, Study of the $2Cu_2S + GeSe_2 \leftrightarrow 2Cu_2Se + GeS_2$ reciprocal system and thermodynamic properties of the $Cu_8GeS_{6-x}Se_x$ solid solutions, J. Alloys Compd. 691 (2017) 255–262, https://doi.org/10.1016/j.jallcom.2016.08.251.

[55] M. Onoda, H. Wada, A. Sato, M. Ishii, Low-temperature forms of superionic conductors, Cu_8GeS_6 and Ag_7TaS_6, and ion conduction path, J. Alloys Compd. 383 (2004) 113–117, https://doi.org/10.1016/j.jallcom.2004.04.018.

[56] W.F. Kuhs, R. Nitsche, K. Scheunemann, The argyrodites — A new family of tetrahedrally close-packed structures, Mater. Res. Bull. 14 (1979) 241–248, https://doi.org/10.1016/0025-5408(79)90125-9.

[57] M. Onoda, X.-A. Chen, K. Kato, A. Sato, H. Wada, Structure refinement of Cu_8GeS_6 using X-ray diffraction data from a multiple-twinned crystal, Acta Crystallogr. Sect. B Struct. Sci. 55 (1999) 1109–1109. 10.1107/S0108768199012938.

[58] M. Ishii, M. Onoda, K. Shibata, Structure and vibrational spectra of argyrodite family compounds Cu_8SiX_6 (X=S, Se) and Cu_8GeS_6, Solid State Ionics 121 (1999) 11–18, https://doi.org/10.1016/S0167-2738(98)00305-1.

[59] D. Brown, The Chemical Bond in Inorganic Chemistry: The Bond Valence Model, 1st ed., Oxford University Press, New York, NY, 2002.

[60] B.H. Toby, R.B. Von Dreele, GSAS-II : the genesis of a modern open-source all purpose crystallography software package, J. Appl. Crystallogr. 46 (2013) 544–549, https://doi.org/10.1107/S0021889813003531.

[61] O.V. Parasyuk, L.V. Piskach, Y.E. Romanyuk, I.D. Olekseyuk, V.I. Zaremba, V. I. Pekhnyo, Phase relations in the quasi-binary Cu_2GeS_3–ZnS and quasi-ternary Cu_2S–Zn(Cd)S–GeS_2 systems and crystal structure of Cu_2ZnGeS_4, J. Alloys Compd. 397 (2005) 85–94, https://doi.org/10.1016/j.jallcom.2004.12.045.

[62] M. Dimitrievska, A. Fairbrother, X. Fontané, T. Jawhari, V. Izquierdo-Roca, E. Saucedo, A. Pérez-Rodríguez, Multiwavelength excitation Raman scattering study of polycrystalline kesterite Cu_2ZnSnS_4 thin films, Appl. Phys. Lett. 104 (2014), https://doi.org/10.1063/1.4861593.

[63] M. Dimitrievska, F. Boero, A.P. Litvinchuk, S. Delsante, G. Borzone, A. Perez-Rodriguez, V. Izquierdo-Roca, Structural Polymorphism in Kesterite Cu_2ZnSnS_4: Raman Spectroscopy and First-Principles Calculations Analysis, Inorg. Chem. 56 (2017) 3467–3474, https://doi.org/10.1021/acs.inorgchem.6b03008.

[64] M.Y. Valakh, O.F. Kolomys, S.S. Ponomaryov, V.O. Yukhymchuk, I.S. Babichuk, V. Izquierdo-Roca, E. Saucedo, A. Perez-Rodriguez, J.R. Morante, S. Schorr, I. V. Bodnar, Raman scattering and disorder effect in Cu_2ZnSnS_4, Phys. Status Solidi - Rapid Res. Lett. 7 (2013) 258–261, https://doi.org/10.1002/pssr.201307073.

[65] E. Garcia-Llamas, M. Guc, I.V. Bodnar, X. Fontané, R. Caballero, J.M. Merino, M. León, V. Izquierdo-Roca, Multiwavelength excitation Raman scattering of $Cu_2ZnSn_{1-x}Ge_x(S, Se)_4$ single crystals for earth abundant photovoltaic applications, J. Alloys Compd. 692 (2017) 249–256, https://doi.org/10.1016/j.jallcom.2016.09.035.

[66] A. Escobedo Morales, E. Sánchez Mora, U. Pal, Use of diffuse reflectance spectroscopy for optical characterization of un-supported nanostructures, Rev. Mex. Física S. 53 (2007) 18–22.

[67] E. Garcia-Llamas, J.M. Merino, R. Serna, X. Fontané, I.A. Victorov, A. Pérez-Rodríguez, M. León, I.V. Bodnar, V. Izquierdo-Roca, R. Caballero, Wide band-gap tuning $Cu_2ZnSn_{1-x}Ge_xS_4$ single crystals: Optical and vibrational properties, Sol. Energy Mater. Sol. Cells 158 (2016) 147–153, https://doi.org/10.1016/j.solmat.2015.12.021.

[68] D.B. Khadka, J.H. Kim, Band gap engineering of alloyed $Cu_2ZnGe_xSn_{1-x}Q_4$ (Q = S, Se) films for solar cell, J. Phys. Chem. C 119 (2015) 1706–1713, https://doi.org/10.1021/jp510877g.

[69] H.J. Shim, U.V. Ghorpade, M.P. Surywanshi, M. Gang, J.H. Kim, Studies on the influence of etching solution on the properties of $Cu_2ZnSn(S, Se)_4$ thin film solar cells, Thin Solid Films 670 (2019) 1–5, https://doi.org/10.1016/j.tsf.2018.11.042.

[70] G. Rey, G. Larramona, S. Bourdais, C. Choné, B. Delatouche, A. Jacob, G. Dennler, S. Siebentritt, On the origin of band-tails in kesterite, Sol. Energy Mater. Sol. Cells 179 (2018) 142–151, https://doi.org/10.1016/j.solmat.2017.11.005.

[71] E. Hajdeu-Chicarosh, Variable-Range Hopping Conduction in the Kesterite and Wurtzstannite Cu_2ZnGeS_4 Single Crystals, Surf. Eng. Appl. Electrochem. 54 (2018) 279–285, https://doi.org/10.3103/S1068375518030055.

[72] E. Hajdeu-Chicarosh, M. Guc, K. Neldner, G. Gurieva, S. Schorr, E. Arushanov, K. G. Lisunov, Mechanisms of conductivity and energy spectrum of near-edge holes in Cu_2ZnSnS_4 powder samples, J. Alloys Compd. 703 (2017) 315–320, https://doi.org/10.1016/j.jallcom.2017.01.352.

[73] Y. Fan, G. Wang, R. Wang, B. Zhang, X. Shen, P. Jiang, X. Zhang, H. Gu, X. Lu, X. Zhou, Enhanced thermoelectric properties of p-type argyrodites Cu_8GeS_6 through Cu vacancy, J. Alloys Compd. 822 (2020), 153665, https://doi.org/10.1016/j.jallcom.2020.153665.